# Numerical modelling and comparison of the temporal evolution of mantle and tails surrounding rigid elliptical objects in simple shear regime under stick and slip boundary conditions

Kieran F. Mulchrone [a,*], Soumyajit Mukherjee [b]

[a] Department of Applied Mathematics, University College, Cork, Ireland
[b] Department of Earth Sciences, Indian Institute of Technology Bombay, Powai, Mumbai 400 076, Maharashtra, India

## ARTICLE INFO

## ABSTRACT

Structures associated with rigid inclusions are a rich source of evidence to understand the local deformation regime. The behaviour of rigid objects in modelled here as being immersed in a linear Newtonian fluid with either (i) a stick boundary condition (continuity of stress and velocity across the boundary) or (ii) a slip boundary condition (continuity of boundary normal stress and velocity across the boundary with zero shear stress at the boundary). Of particular interest are the types of structures developed in a concentric region adjacent to the object termed the mantle. A model of the displacement of points around the inclusion comprises a set of ordinary differential equations which are solved numerically. A comprehensive set of simulations for a variety of mantle sizes, object aspect ratios, initial orientations as well as different boundary conditions has been performed. A comparison between natural examples and model output indicates a level of consistency. The resulting structures differ in detail and in a broader sense. In general $\delta$-type structures only develop when stick boundary conditions are in operation. In contrast, $\sigma$-type structures at high strain are restricted to slip boundary conditions. Slip conditions also tend to be the source of complex mantle types involving more than one generation of mantle structures or wings. Furthermore, our model indicates that using asymmetry of orientation of objects relative to the shear direction may be problematic when used alone, particularly if stick boundary conditions prevail but that together with mantle structures there is less chance of confusion.

*"Hard inclusions (e.g. mineral grains) in a relative weaker matrix form one class of structures that have received much attention for the potential wealth of information stored in them, such as sense of shear, kinematic vorticity number, distinguishing different deformation events, finite strain, etc".*

[Griera et al. (2013)]

## 1. Introduction

The study of ductile shear zones is crucial in tectonics and earthquake studies (Regenauer-Lieb and Yuen, 2003). Couette flow in fluid mechanics (Schlichting and Gersten, 1999), the same as simple shear in structural geology, produces a linear velocity profile when the shear zone boundaries are parallel (Mukherjee, 2012; Ramsay, 1980). Mulchrone and Mukherjee (2019) in their Fig. 1 reviewed different kinds of shear zones relevant to structural geology. Ductile shear sense indicators are a key structure used by structural geologists to determine

shear sense and understand deformation type (Passchier and Trouw, 2005; Dutta and Mukherjee, 2019). Behaviour of competent objects, such as porphyroclasts, in various deformation regimes (Ghosh and Sengupta, 1973) and their degree of bonding with the matrix (Ildefonse et al., 1992; Odonne, 1994) have been discussed broadly in previous literature. However, the detailed mechanism of the development of mantle structures and the types of structures developed under differing boundary conditions has not been addressed.

In this paper, we study and compare the development of mantle structures around rigid elliptical objects in a simple shear flow in the case of stick and slip boundary conditions. We first review relevant work in the literature and then describe the modelling approach used. We undertook a comprehensive series of numerical simulations taking account of a variety of boundary and initial conditions. Results are mainly presented in graphical form. Furthermore, we consider a selection of natural examples for comparison before drawing conclusions.

---
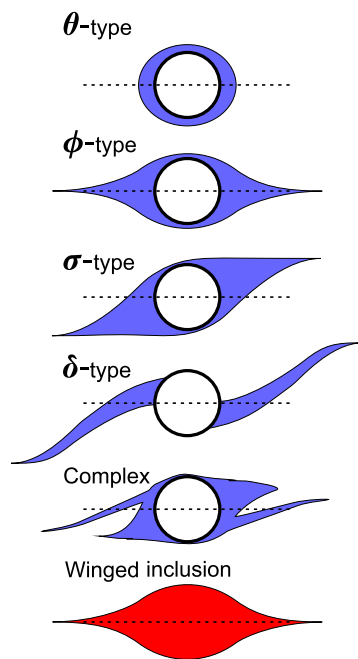
**Fig. 1.** Schematic illustration of the various types of mantle structure observed in nature. The shear sense is dextral and the shear direction is indicated by the dashed line. A circular rigid core is surrounded by blue mantle material which is assumed to have a viscosity similar to that of the surrounding material. The bottom structure is a winged inclusion which is composed entirely of material with uniform viscosity different to that of the surrounding material and is usually more competent (it is coloured differently to distinguish it).

## 2. Previous work

The behaviour of rigid and non-rigid objects during deformation has been of considerable interest to structural geologists because their rotational characteristics can potentially help understand the type of deformation which can scale up to map scale tectonic interpretations (Marques et al., 2014). Typically in this type of analysis a steady state deformation is assumed, meaning that the velocity gradient tensor is constant. In spite of this simplification, many insights have been gained into types of deformation history and how they might be recognized in nature (Fossen and Tikoff, 1993; Tikoff and Fossen, 1993, 1995, 1999; Fossen and Cavalcante, 2017). For example, the relationship between foliations, lineations and vorticity indicators can be used to determine the broad structure of the velocity gradient tensor (Tikoff and Fossen, 1999) and thus understand deformation history in 3D. Clearly then, understanding how to correctly interpret populations of rigid objects and structures such as mantles and tails around rigid objects is crucial to tectonic analysis.

Modelling, almost by definition, involves abstraction and simplification. However, the inspiration for the models developed below (see Section 3) are mantled objects where the mantle surrounding the core can be recrystallized minerals, a reaction product of the core itself, or strain shadows (Fig. 5.20 of Passchier and Trouw (2005)). Typically porphyroclasts are feldspar surrounded by a matrix of quartz-feldspar-mica or orthopyroxene in peridotite or dolomite in calcite (Passchier and Trouw, 2005). Principle factors controlling the geometry of the evolving mantle are deformation type, e.g. pure versus simple shear, object aspect ratio and boundary conditions and the rheology of the matrix is thought to negligible (Ildefonse and Mancktelow, 1993; Bons et al., 1997; Griera et al., 2013).

Five varieties of mantled objects have previously been identified (Passchier and Simpson, 1986):

1. $\Theta$-type: display no wings but mantle may bulge.

2. $\phi$-type: exhibit wings on each side of the object which are stretched out parallel to the shear plane and each other.
3. $\sigma$-type: have a wedge-shaped mantle with stair stepping wings.
4. $\delta$-type: the median line of wings cross the shear plane, with or without stair stepping.
5. Complex-type: multiple generations of wings.

A schematic illustration of the different varieties is presented in Fig. 1. $\Theta$-type structures are typically symmetric but do not exhibit wings whereas $\phi$-type structures exhibit symmetric wings aligned with the shear direction. Both $\sigma$ and $\delta$-type structures comprise asymmetric wings with respect to the shear direction, however, the former exhibit a stair stepping geometry and the latter are thinner, more curved and cross the shear plane. Complex structures come in many varieties but may exhibit two or more features from $\Theta$, $\phi$, $\sigma$ or $\delta$ structures. The final structure type shown in Fig. 1 are winged inclusions (Grasemann and Dabrowski, 2015). Although geometrically similar to mantled structures, a key difference is that they do not form around a rigid core. The material in a winged inclusion is idealized as having uniform viscosity different to that of the surrounding material. For example, they may be initially formed as segments of a boudinaged layer.

Experimental and numerical evidence indicates that it is the flow pattern (eye-shaped or bow-tie shaped) around the object that determines the variety of mantle structure observed (Passchier et al., 1993; Passchier and Trouw, 2005). Furthermore an additional flow pattern named cats eye shaped has been identified by Marques et al. (2005b, 2014). A schematic illustration of each flow pattern is presented in Fig. 2. Eye patterns are associated with stick boundary conditions in simple shear whereas bow tie patterns are associated with stick boundary conditions in confined flow (Marques et al., 2005b, 2014). On the other hand, cat eye patterns were found (Marques et al., 2005a) specifically in relation to slip boundary conditions.

The phenomenon of mantled structures has been approached from both analogue experimental and theoretical perspectives. Theoretical work has tended to focus on the situation where the object is strongly bonded to the matrix (referred to as a stick boundary condition here) whereas analogue models have considered both bonded and loosely bonded (referred to as a slip boundary condition here) objects (Marques et al., 2014).

Experimental evidence suggests that wings tend to develop only when the viscosity contrast between the materials in the mantle and the surrounding matrix is small and $\delta$-type wings form only when the mantle is relatively thin (Passchier and Sokoutis, 1993). Furthermore, Passchier and Sokoutis (1993) found that $\delta$-type wings cannot develop under slip as the object does not rotate through the shear plane but can develop under stick whereas highly stretched $\sigma$-type wings are a feature of slip. Experimental work using circular inclusions by Bose and Marques (2004) also found that stick conditions are required for $delta$-type wing development and that $\sigma$-type structures can occur under both stick and slip. Additionally, stair stepping was found to occur in both $\delta$ and $\sigma$-type wings but was more pronounced under slip conditions. Marques et al. (2014) review a large amount of important experimental work on the behaviour of deformable and non-deformable inclusions with stick and slip conditions, and during confined and unconfined deformation conditions.

Numerical investigations typically use the finite element method to investigate structures developed for rigid inclusions immersed in Newtonian, power law and non-Newtonian viscous fluids (Bons et al., 1997; Pennacchioni et al., 2000; Marques et al., 2005a; Schmid and Podladchikov, 2005; Grasemann and Dabrowski, 2015). Bons et al. (1997) focus on flow around a circular inclusion and found that boundary conditions rather than matrix rheology determined the flow type. Pennacchioni et al. (2000) examined in detail the flow pattern in the matrix surrounding circular objects for stick and slip boundary conditions and found that bow-tie type patterns occur for stick conditions independent of the value of the power law exponent in the power-law

eye pattern

bow tie pattern

cat eye pattern
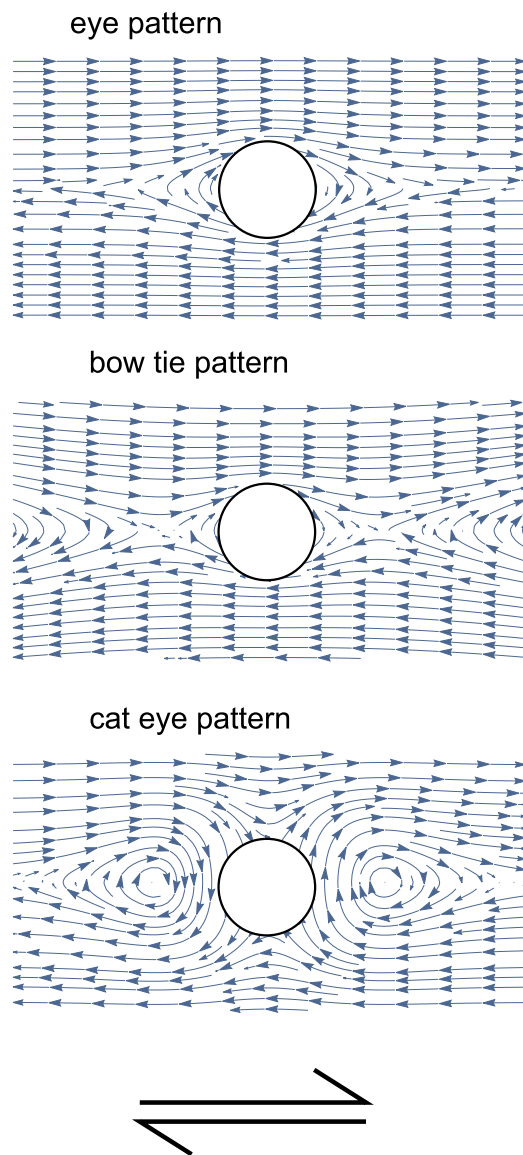
**Fig. 2.** Schematic illustration of suggested flow patterns around circular rigid objects.

matrix. In contrast when slip occurs a different flow pattern is observed which depends strongly on the properties of the matrix. However, they do not consider the evolution of tail geometry over time. Marques et al. (2005a) model the lack of coherence between the object and matrix by a permanent low viscosity layer and considered different shapes (circle, square, lozenge, ellipse, rectangle and parallelogram). They found neither bow-tie nor eye-type flow patterns but instead found "cats eye"-shaped flow patterns. Furthermore they found antithetic rotation of objects and the existence of stable equilibrium object orientations. Schmid and Podladchikov (2005) use a similar set-up to Marques et al. (2005a) and found stable object orientations and in addition, related physical attributes of mantled objects to effective viscosity contrast between mantle and matrix, mantle production rate and total shear strain.

Recently, the development of winged inclusions was numerically investigated (Grasemann and Dabrowski, 2015), and here pinch and swell type structures (i.e. with pre-existing wings) are the initial geometry. It is important not to confuse winged inclusions and mantled porphyroclasts for correct determination of shear sense.

In series of contributions (Mandal et al., 2000, 2001; Samanta et al., 2003; Mandal et al., 2003), the development of mantled objects was

studied using a 2D equivalent of the model of Jeffery (1922). In one model object material was converted to mantle material at a fixed rate during deformation (Mandal et al., 2000), whereas Mandal et al. (2001) focused on particle paths and finite strain patterns. They found that factors affecting the geometry of mantles were object aspect ratio, rate of object reduction and flow vorticity. Mantles of type $\delta$, $\phi$ and $\sigma$ were produced as the rate of object reduction increases. They also consider the effects of multiple particle interaction (Samanta et al., 2003). In a later contribution, the instantaneous rotation of rigid inclusions in an anisotropic matrix was analysed (Mandal et al., 2005).

A rectangular rigid object without any mantle, similar to naked objects in rocks, was used in analogue models to investigate the effect of slip-boundary condition (Ildefonse and Mancktelow, 1993). The strain condition around the object was found to be markedly different from that of the no-slip boundary condition. The object that stays mantled is usually less deformed or undeformed (Bose and Marques, 2004). The geometry of tails around objects in a matrix under simple shear depend on (i) mantle production rate, (ii) deformation rate, (iii) radius of circular mantle surrounding the object, (iv) shape of the object — whether circular or rectangular, (v) rate of object size reduction (review in Ildefonse and Mancktelow (1993); Mandal et al. (2000)). Additionally, Trouw et al. (2010) based on qualitative studies of thin-sections comment that higher temperature shear zones produce more symmetric objects (such as Fig. 13a in Mukherjee (2017)). Bellot et al. (2002) consider symmetric ("category-i" of Bjornerud (1989)) of pressure shadows/tails (and pressure fringes) as products of pure shear (also see Ishii et al. (2007)). Continuous simple shear can alter an asymmetric shear sense indicator into a symmetric structure and then again into the former shape (Passchier, 1984; Mukherjee, 2017). On progressive deformation, wings might alter morphologically but the objects simply reduce size (Passchier and Trouw, 2005).

The issue of stick or slip boundary conditions may also have a bearing on larger scale structures. Shear zones that do not reach Earth's surface are entirely laterally confined, suggesting that no-slip boundary conditions should apply in general for small- to mesoscale structures (Schrank et al., 2008). Perhaps for this reason the 'no-slip' boundary condition is assumed in most structural geological contexts. Mulchrone and Mukherjee (2016) discuss velocity and shear heat profiles for slip boundary condition in simple shear zones. Slip boundary conditions may be facilitated by the presence of fluids or partial melts (Hollister and Crawford, 1986; Boudier and Al-Rajhi, 2014). Analogue models often produce partial slip conditions even when trying to implement a perfect no slip condition (Frehner et al., 2011).

## 3. Modelling mantles around rigid objects with stick and slip boundary conditions

The types of object rotation demonstrated in the present work are expected to occur if the rock matrix behaves either as a linear or a power law viscous fluid. For an elastoplastic matrix, however, such a rotation is not possible (Griera et al., 2013).

The mathematical models considered here are concerned with the motion of a rigid ellipse, with axial ratio $R$, immersed in an isotropic viscous fluid (Jeffery, 1922; Mulchrone and Walsh, 2006; Mulchrone, 2007a,b). It is a fundamental assumption of these models that the rigid object is isolated from and not interfered with by neighbouring objects. Additionally it is assumed that the flow is unconfined in the sense that at large distances from the object the perturbations to the flow due to the presence of the object are effectively zero and negligible. In practical terms this means that width of the shear zones ought to be of the order 20 times that of the long axis of the object. Iacopini et al. (2011) provide a discussion of the validity of these assumptions in a geological context.

In deriving the solution for the motion of a rigid ellipse with stick or 'no slip' boundary conditions Jeffery (1922) also determined the form
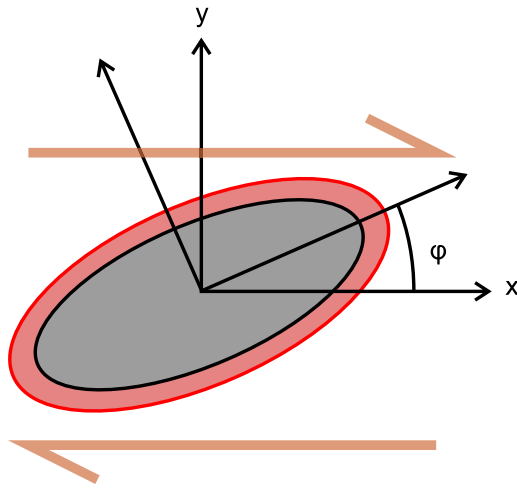
**Fig. 3.** Diagram illustrating the set up of the model. A rigid object of known axial ratio $R = \frac{a}{b}$, where $a$ is the length of the long axis and $b$ that of the short axis. The object makes an angle $\phi$ with the positive $x$-axis. The black curve is the outer boundary of the rigid object and the red curve is the outer bound of the area modelled as the mantle. Dextral shear sense is illustrated.

of the perturbed flow around the object. A stick boundary condition means that the velocity and stress of the external flow and internal flow are equal at the boundary. The long axis of the rigid ellipse makes an angle of $\phi$ with the positive $x$-axis which is parallel to the shear direction. The mantle is modelled as a band of material directly adjacent to the rigid object (see Fig. 3), which is delimited by an elliptical curve outside of the rigid object. The axial ratio of the mantle region is identical to that of the rigid object. The evolution of the mantle curve is determined by the perturbed flow outside the object. Thus we assume that the mantle material behaves in the same way as any other material beyond the rigid elliptical object. In particular, the solution of Mulchrone and Walsh (2006) (see their eqs. 58–61) where $\mu_r = 0$ (the ratio of the external to internal viscosities, equivalent to the solution of Jeffery (1922)) is used.

A solution for the motion of a rigid object with a slip boundary condition has already been derived (Mulchrone, 2007a). A slip boundary condition means that boundary normal components of velocity and stress are equal and shear stress is zero at the boundary. The flow adjacent to the slipping elliptical object can be determined using the perturbed velocity solution given by Mulchrone (2007a).

In each case a large system of ordinary differential equations needs to be solved. Code written in the technical computing environment of Mathematica (version 12) was used to solve these equations and to produce the graphical solutions presented. In each model the shear strain rate is taken to be unity, which is immaterial because the results are presented in terms of finite shear strain. Furthermore, because the object is rigid (effectively infinite viscosity) the viscosity of the surrounding material is irrelevant. In all model solutions a dextral simple shear is applied as the background (i.e. far-field) flow.

The rotational behaviour of rigid objects differs quite significantly depending on the type boundary condition applied (Mulchrone and Walsh, 2006; Mulchrone, 2007a). The rotation rate for a stick boundary condition is (Mulchrone, 2007a):

$$\frac{d\phi}{dt} = \frac{\dot{\gamma}}{2}\left(\frac{(R^2-1)\cos 2\phi}{R^2+1} - 1\right) \tag{1}$$

where $\dot{\gamma}$ is the rate of shear strain. This equation implies that the rigid object rotates continuously and speeds up or slows down depending on $R$ and $\phi$. If $\dot{\gamma} > 0$ the slowest rotation occurs for $\phi = 0$ and the object rotates fastest for $\phi = \frac{\pi}{2}$. On the other hand with a slip boundary condition the rotation rate is (Mulchrone, 2007a):

$$\frac{d\phi}{dt} = \frac{\dot{\gamma}}{2}\left(\frac{(R+1)\cos 2\phi}{R-1} - 1\right). \tag{2}$$

This equation admits two orientations where the object does not rotate, one stable and one unstable. For $\dot{\gamma} > 0$ these orientations are:

$$\phi^+ = \frac{1}{2}\cos^{-1}\left(\frac{R-1}{R+1}\right) \tag{3}$$

$$\phi^- = -\frac{1}{2}\cos^{-1}\left(\frac{R-1}{R+1}\right). \tag{4}$$

For $\phi^+$ the orientation is stable in the sense that after a small perturbation away from this orientation the object will rotate back into the stable orientation whereas for $\phi^-$ the orientation is unstable and any perturbation away from it will result in the object rotating into the stable orientation. Thus it is almost certain that all objects will rotate into the direction of the stable orientation. The level of shear strain required for an object to reach the stable orientation depends on $R$ and the initial orientation ($\phi_0$). Taking $\phi_0$ far from $\phi^+$ then for $R = 2$ the stable orientation is almost attained at a shear strain of 3, whereas for $R = 10$ it takes a shear strain of 6.

A notable behaviour of objects with slip boundary conditions is the ability to rotate both synthetically and antithetically. Considering the interval $(0, 180°)$ then synthetic rotation occurs for $0 \le \phi < \phi+$ and $\phi^- < \phi \le 180°$, whereas antithetic rotation occurs for $\phi^+ < \phi < \phi^-$.

It is instructive to consider and compare the flow around rigid inclusions in the cases of stick and slip (see Figs. 4 and 5). In the case of a stick boundary condition (Fig. 4) there is a continuity of the velocity field between outside and inside the object, demanded by the boundary condition. Because the elliptical object is executing a rigid rotation, the velocity field inside consists of circular arcs. In all cases the sense of rotation is consistent with the overall dextral shear sense imposed on the model. Outside the object the velocity field is significantly perturbed. The flow is perfectly symmetrical for $\phi = 0°$ and $90°$ and is somewhat asymmetrical for $0° < \phi < 90°$ and $90° < \phi < 180°$. There are no stagnation (where the velocity is zero) points present.

The velocity fields in the case of a slip boundary condition are quite different (Fig. 5). The flow is typically disjointed between the inside and outside of the object, however, the boundary normal velocity components are equal. For $\phi = 45°$ and $135°$ the flow fields are continuous and identical to the velocity field in the stick case. The internal velocity field consists of circular arcs due to rigid rotation however it can oppose the sense of shear (see for example $\phi = 150°, 165°, 0°, 15°, 30°$). A pair of stagnation points appear adjacent to the rigid object for certain angles (see $\phi = 60°$ and $120°$, for example). The velocity field is symmetric for $\phi = 0°$ and $90°$ but demonstrates a much great asymmetry away from these values (see $\phi = 30°$ and $150°$).

Given the differences in the velocity fields for stick and slip conditions it is reasonable to expect differences in the geometry of mantles developed. Furthermore, during the course of deformation with a stick boundary condition, the object undergoes continual rigid body rotation as the mantle geometry changes. On the other hand, the case of slip, the object relatively quickly rotates into a stable orientation and stops rotating, but the mantle material continues to deform.

## 4. Results

In this section the evolution of mantle geometries under stick and slip conditions are examined and compared in a simple shear regime. In particular, the effect of (i) aspect ratio ($R$) (ii) initial orientation ($\phi_0$) and (iii) mantle size is studied. Mantle size is quantified as the difference between length of the long axis of the mantle region ($a_m$) and that of the rigid ellipse ($a_o$), divided by the length of the long axis of the ellipse ($a_0$). Thus mantle size is given by $\frac{a_m}{a_0} - 1$. For example, if the mantle region has long axis of size 11 and the ellipse has long axis of size 10 then the mantle size is given as 0.1 or 10%. The aspect ratios investigated are $R = 1.25, 1.66, 2.5, 5, 10$, the initial orientations ($\phi_0$) vary from 0° to 360° in steps of 5.625° ($\frac{\pi}{32}$ radians) and mantle sizes are 10%, 20%, 30% and 40%. For each combination of parameters the system was numerically solved up to a total shear strain ($\gamma$) of 10.
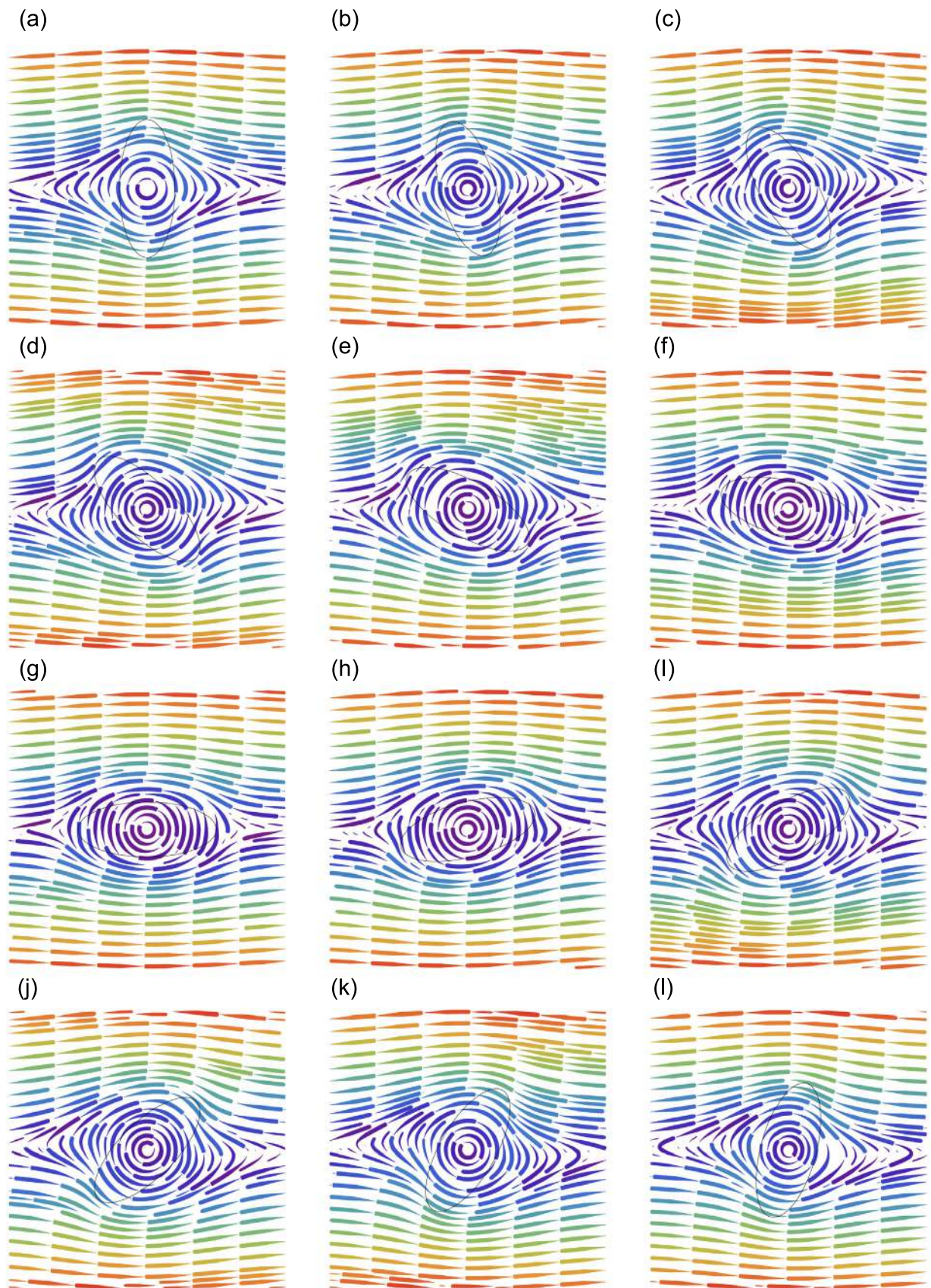
**Fig. 4.** Flow field inside and around the rigid object with a stick boundary condition. A thin black curve delimits the extent of the rigid ellipse ($R = 2.5$). Diagrams illustrate the velocity field for ellipse angles $\phi = 90, 105, 120, 135, 150, 165, 0, 15, 30, 45, 60, 75$ left to right and top to bottom (a to l). Velocity direction is indicated by the fat end of the markers. Red represents the fastest velocity and dark blue the slowest velocity. (For interpretation of the references to colour in this figure legend, the reader is referred to the web version of this article.)
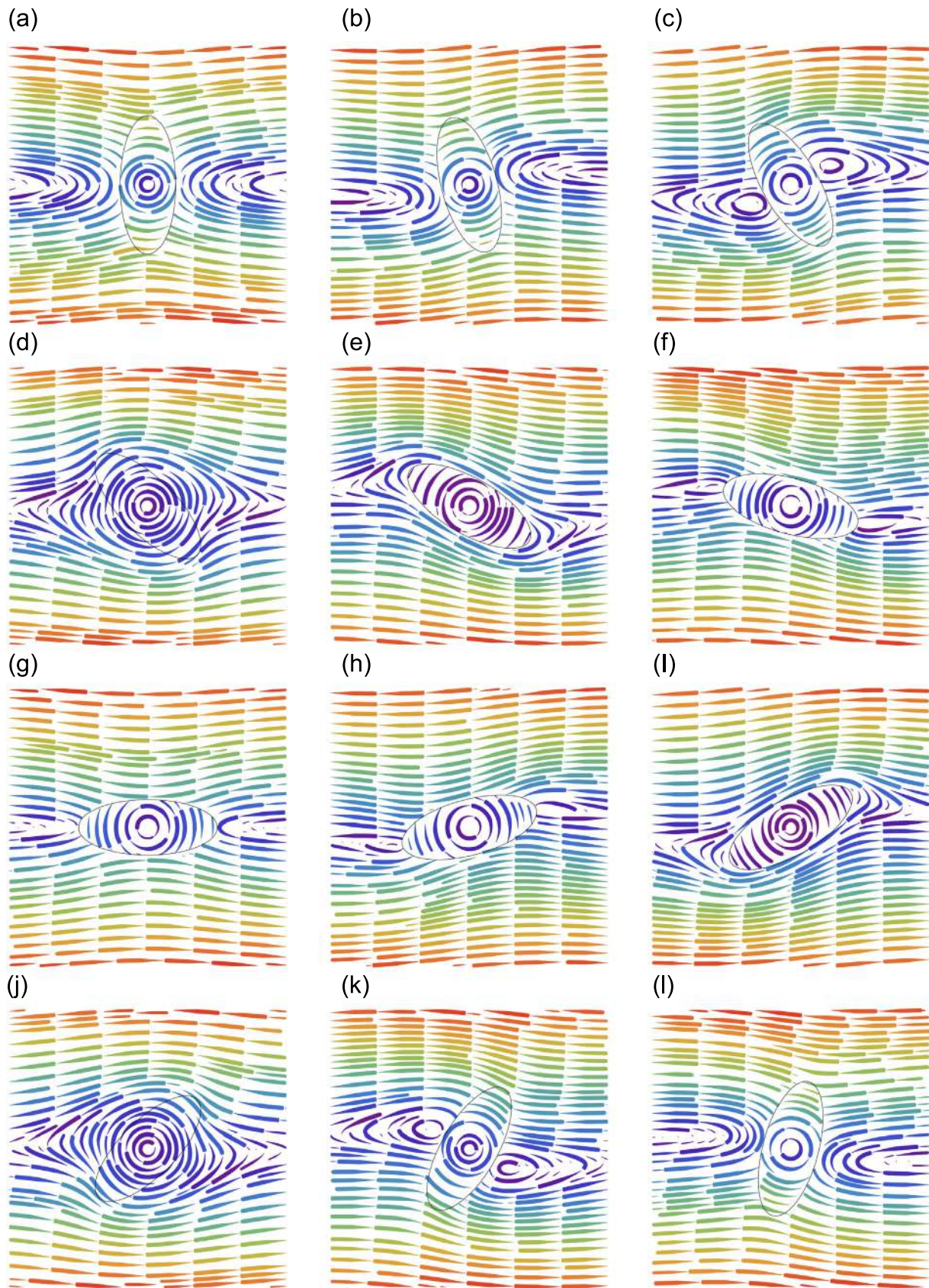
**Fig. 5.** Flow field inside and around the rigid object with a slip boundary condition. A thin black curve delimits the extent of the rigid ellipse ($R = 2.5$). Diagrams illustrate the velocity field for ellipse angles $\phi = 90, 105, 120, 135, 150, 165, 0, 15, 30, 45, 60, 75$ left to right and top to bottom (a to l). Velocity direction is indicated by the fat end of the markers. Red represents the fastest velocity and dark blue the slowest velocity. (For interpretation of the references to colour in this figure legend, the reader is referred to the web version of this article.)
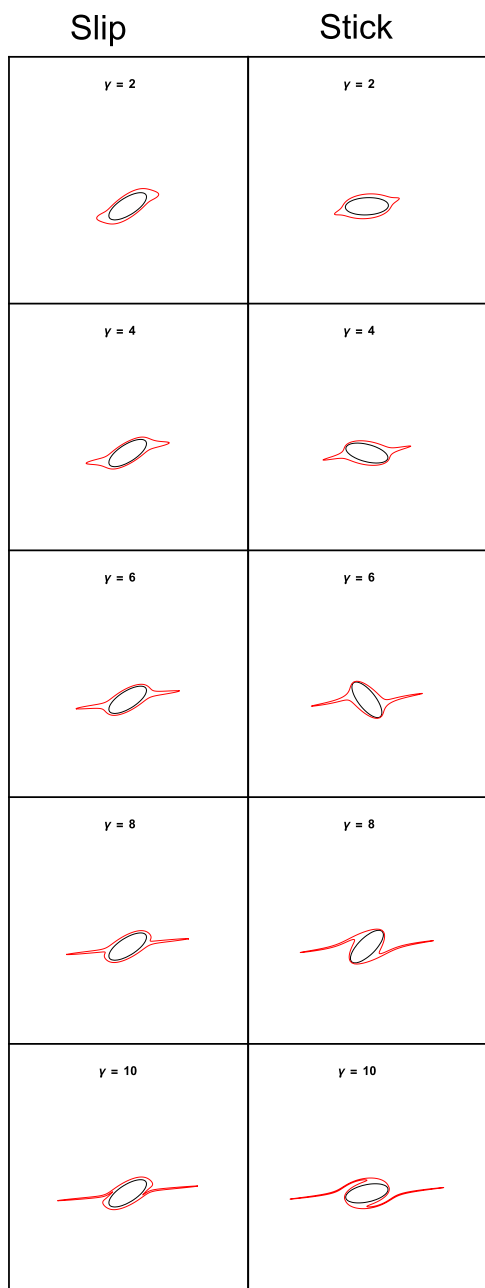
**Fig. 6.** Side by side illustration of slip versus stick mantle structures for mantle size 20%, $R = 2.5$ and $\phi_0 = 22.5°$.
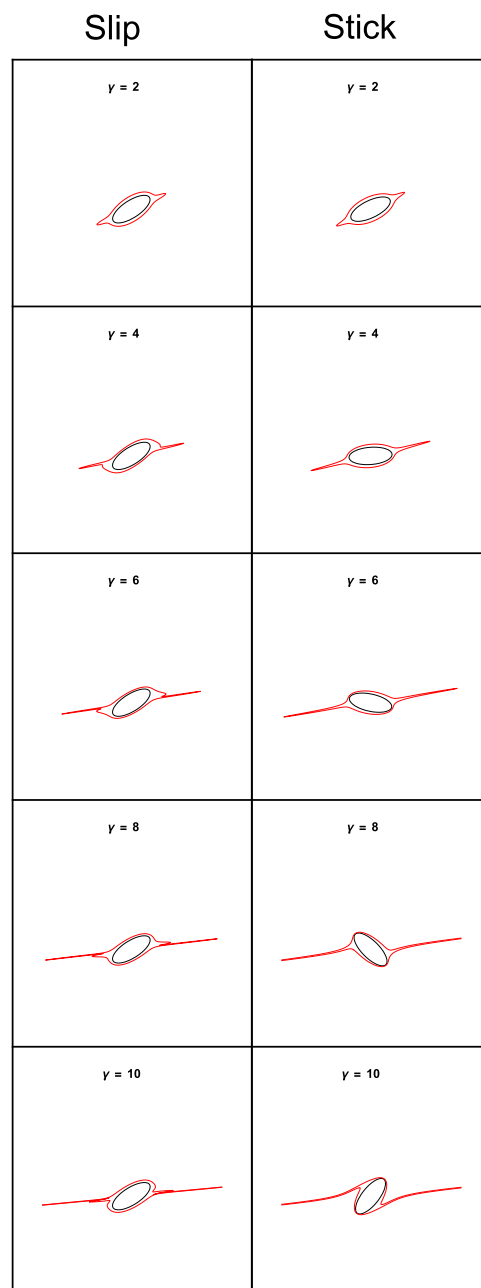


**Fig. 7.** Side by side illustration of slip versus stick mantle structures for mantle size 20%, $R = 2.5$ and $\phi_0 = 90.0°$.

Detailed results are presented in an electronic appendix as a series of pdf files. A summary of the results in presented by side comparisons of slip and stick structures for a variety of parameters in Figs. 6 to 13.

In the case of slip boundary conditions and relatively high aspect ratio the predominant morphology is $\sigma$-type mantles (see Fig. 6) especially at lower strain levels. Stair stepping is clear at lower shear strain but tends to diminish at higher shear strains. Depending on the initial orientation (see Fig. 7) more complex $\sigma$-type structures where two wings generations are present (e.g. see Fig. 7 for slip with $\gamma = 6$) can develop. This corresponds to complex-type wings in the classification reviewed earlier. By contrast, in the case of stick boundary conditions (see Figs. 6, 7, 10 and 11), only $\delta$-type structures develop with stair stepping.

For lower aspect ratios, i.e. more circular inclusions, the difference between mantles around slip and stick inclusions is less pronounced.

For mantle size = 20% mantles may bulge or produce short wings in both cases (see Fig. 6). However, depending on initial orientation more $\delta$-like structures develop around stick inclusions (see Fig. 9). For mantle size = 40% more extensive, similar wings are produced in both cases (Figs. 12 and 13).

Larger mantle sizes tends to produce more enhanced structures around inclusions. Furthermore, in the case of relatively high aspect ratios, the lengths of wings tends to increase with shear strain. This suggests that by measuring the length of wings systematically across a shear zone may allow a quantitative/qualitative assessment of shear strain variation. This idea was tested for $R = 2.5$ and $\phi_0 = 90°$ in both the slip and stick cases. Using the centre of the elliptical object as the origin, the maximum point in the $x$-direction on the mantle was selected. Shear strain was estimated by the ratio of the $x$ to the $y$ coordinate of the maximum point. Fig. 16 shows the output compared
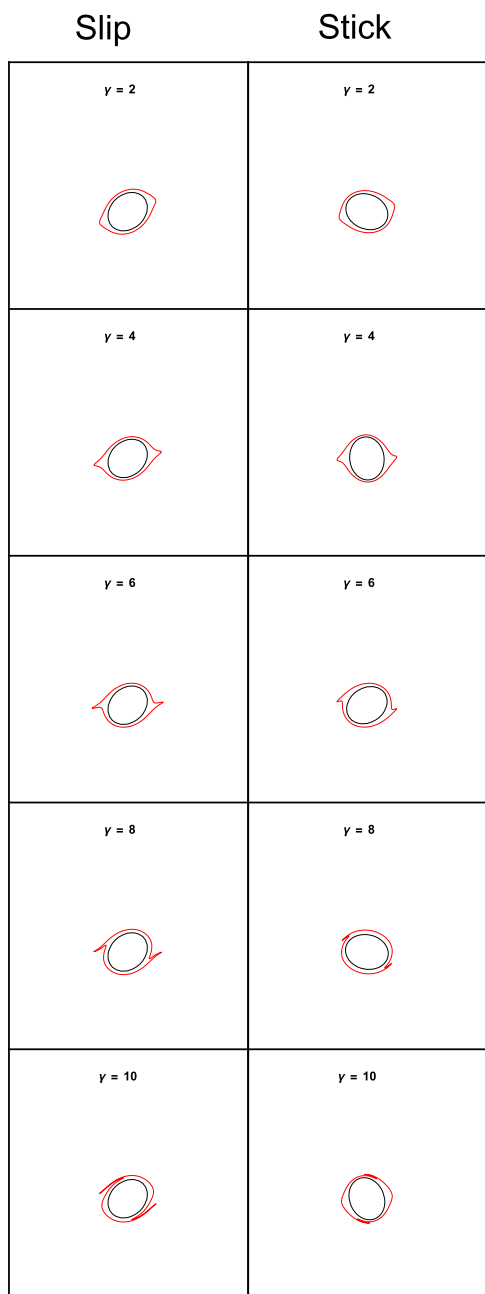
**Fig. 8.** Side by side illustration of slip versus stick mantle structures for mantle size 20%, $R = 1.25$ and $\phi_0 = 22.5°$.
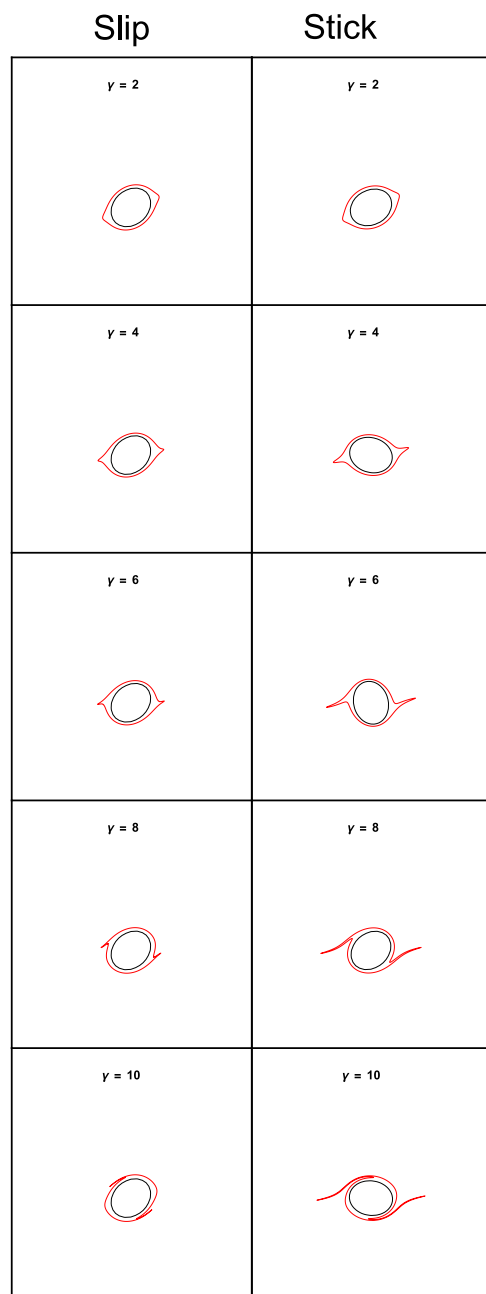


**Fig. 9.** Side by side illustration of slip versus stick mantle structures for mantle size 20%, $R = 1.25$ and $\phi_0 = 90.0°$.

with the actual shear strain in both cases. It is clear that the method is poor for shear strain less than one but for higher shear strains it is remarkably accurate. We reiterate that this approach, according to our results, will only be useful when the elliptical object has a high aspect ratio.

## 5. Application to natural data

The present modelling work can be readily compared with natural examples of sheared clasts with mantle structures where dominantly simple shear deformation has taken place. We consider examples from two locations: (i) Greater Himalayan Crystallines (GHC; Indian Himalaya); and (ii) the Tso Morari Crystalline (TMC) gneiss dome from the Ladakh/Trans-Himalayan range (India). The top-to-S/SW ductile sheared GHC rocks, with a significant simple shear component,

are mostly Precambrian and Proterozoic schists and gneisses metamorphosed to greenschist and amphibolite facies, and Mid-Miocene leucogranites. In addition there are few exposures of granulites and metabasites, and Ordovician orthogneiss (review in Mukherjee (2013b)). The TMC gneiss metamorphosed at amphibolite to granulite facies while extruding from 120 km depth following Poiseuille flow mechanism involving simple shear, which is reflected in meso-scale as extensional ductile shear zones (review in Mukherjee and Mulchrone (2012)).

As the present model considers deformation of an internally rigid core surrounded by a softer deformable rim of a different rheology, we exclude two cases (i) the core and the rim are composed of grains of the same mineral (e.g., rolling structures and/or winged inclusions; Fig. 14a); (ii) mineral fish that are devoid of tails of different materials surrounding them like rims, and the fish themselves
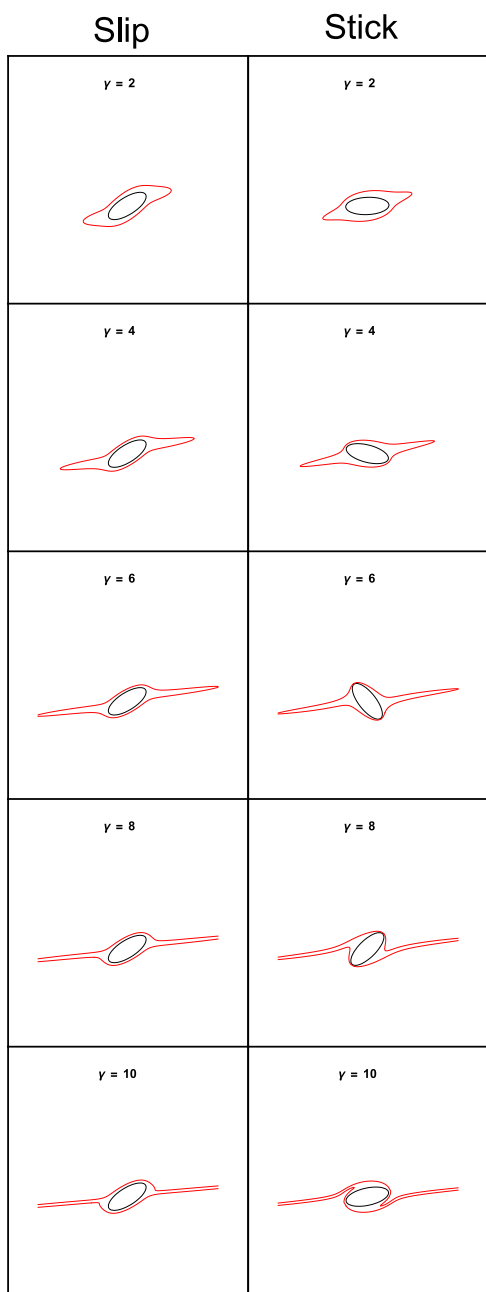
**Fig. 10.** Side by side illustration of slip versus stick mantle structures for mantle size 40%, $R = 2.5$ and $\phi_0 = 22.5°$.
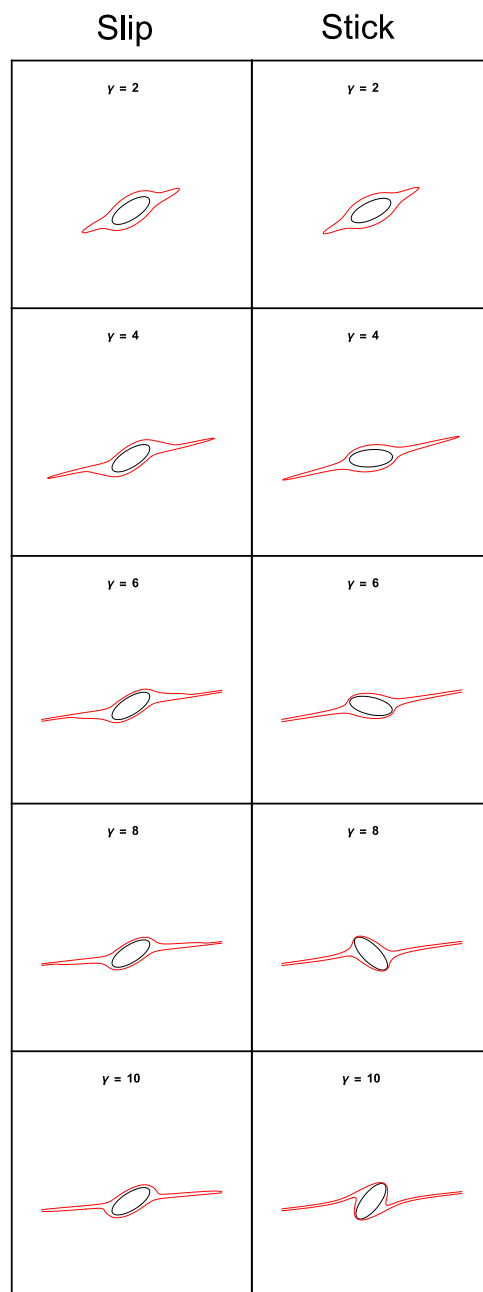


**Fig. 11.** Side by side illustration of slip versus stick mantle structures for mantle size 40%, $R = 2.5$ and $\phi_0 = 90.0°$.

are deformable (Passchier and Trouw, 2005; Mukherjee, 2011). Complex structures can be found around a single core that exhibit tails with $\sigma$ and $\delta$-type features, in both meso- (Fig. 14b) and micro-scales (Fig. 14c). The examples in Figs. 14a and 15d resemble the model output (for example) in Fig. 6 stick $\gamma = 10$ with $\delta$-type characteristics. In contrast the examples in Fig. 14b, c, d and Fig. 15a, b, c are of $\sigma$-type and are more consistent with model output from slip examples (e.g. see Fig. 12 or 13 for $\gamma < 8$).

Of particular interest here are the clearest examples where the foliation around the core is visible (Figs. 14c, 15a,c). As well as appealing to the similarity of the model output, the flow pattern around the core with a slip boundary condition (Fig. 5) is consistent with this pattern. For example consider Fig. 5g, the flow tends to produce and maintain the $\sigma$-type pattern. By contrast, in the case of a stick boundary condition (Fig. 4g) the flow pattern is one whereby a periodic flow around the

core is always present. A $\sigma$-type pattern may initially form but as deformation continues this pattern is smeared into a $\delta$-pattern.

There are several new directions in which "core-mantle research" needs to be furthered: (i) natural shear zones reveal several examples (e.g. Fig. 15c), which are not exactly simulated in any of our models. Perhaps more realistic boundary conditions are required to simulate such structures, for example conditions may switch from stick to slip and back again during deformation. (ii) There are natural cases when the tails and the matrix of a core-mantle structure are folded (Fig. 15d). This may imply post-shear folding of the bulk rock or alternatively the flow regime is not simple shear and has a pure shear component or it may the result of progressive simple shear. Additionally, it might be that local conditions (e.g. rheology, competency or geometry) influence the specifics of the developed structure and requires further investigation.
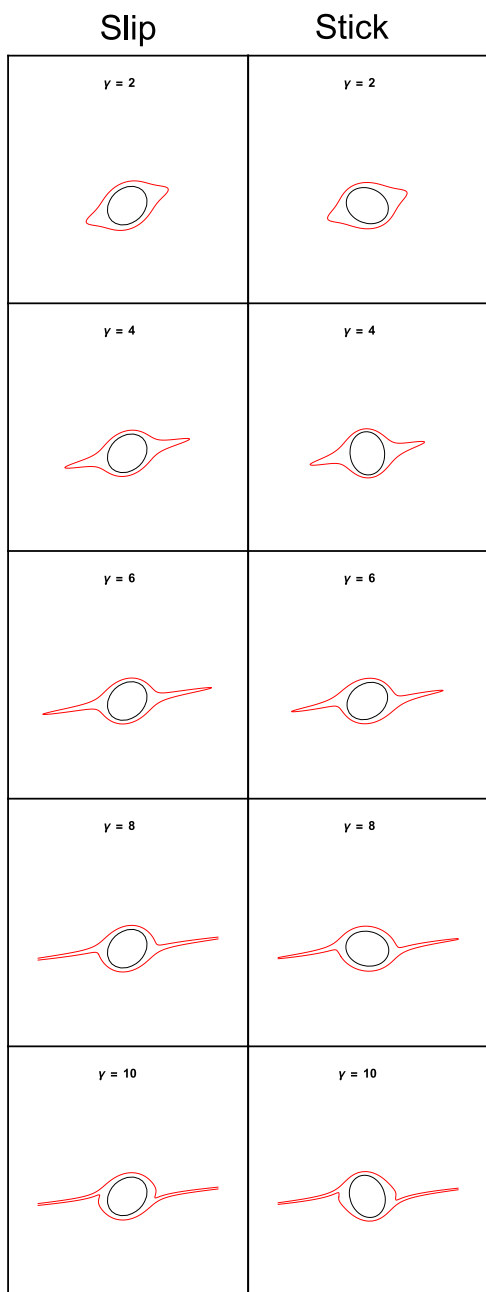
**Fig. 12.** Side by side illustration of slip versus stick mantle structures for mantle size 40%, $R = 1.25$ and $\phi_0 = 22.5°$.
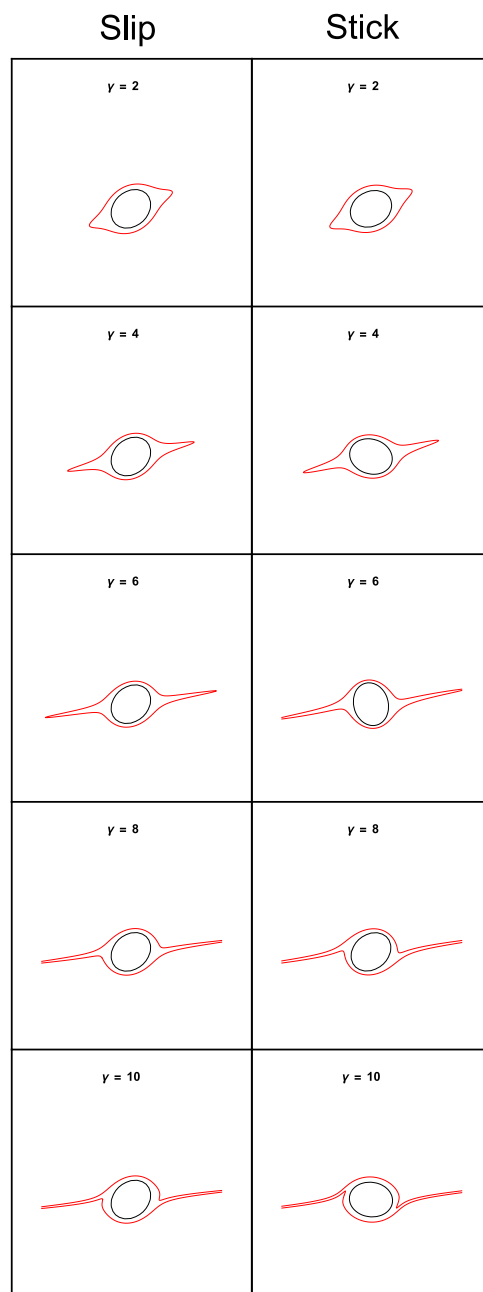


**Fig. 13.** Side by side illustration of slip versus stick mantle structures for mantle size 40%, $R = 1.25$ and $\phi_0 = 90.0°$.

## 6. Discussion and conclusions

The model presented here is based on a continuum approximation of rock behaviour with a linear or Newtonian rheology. In reality, rock behaviour is much more complex. For example, in Fig. 14c the mix of discrete grains of quartz and mica surrounding the garnet core is clearly observed. We emphasize the approximate nature of the model used in this contribution which cannot be expected to exactly reproduce natural structures.

Nevertheless, our results indicate that one of the key differences between mantle structures around slip and stick objects in the development of $\sigma$ or $\delta$ structures respectively. However, this is only true at relatively high shear strains ($\approx \gamma > 8$). At lower shear strains the structures are quite similar. However the presence of $\delta$ structures appears to be a definite indicator of stick boundary conditions. Our model also indicates that in the case of thin mantles and low object aspect ratios structures tend to be muted. This is not the case for higher aspect ratios. In the case of thicker mantles (relative to the object size) notable structures develop independent of aspect ratio.

An important take away from this work is the usefulness of the core-mantle structures in shear sense determination. The geometry of the core should not always be used in isolation for shear sense determination. For example, consider the $\gamma = 6$ stick case in Fig. 10 an elliptical core with its long axis oriented antithetic to the applied dextral simple shear. It is therefore suggested that only the geometry/inclination of the tails (e.g., $\gamma = 6$, stick case in Fig. 10 itself) is used to deduce shear sense. However, when the tail is not well developed then even at high strain (e.g., $\gamma = 10$, stick case in Fig. 8), tails alone may not be a reliable shear sense indicator. A field/lab structural geologist in that case needs to skip that specific core-mantle structure and look for
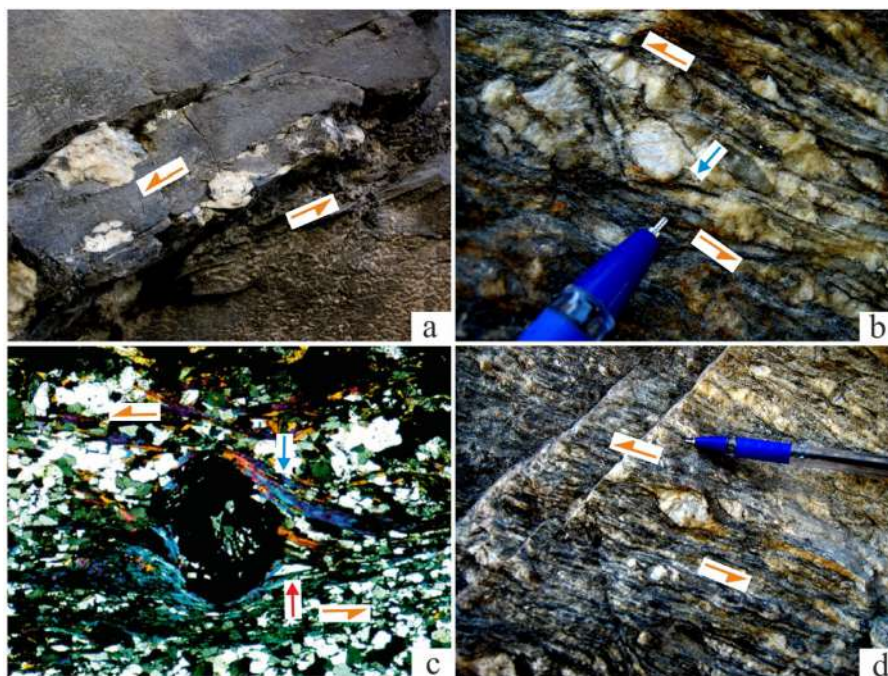
**Fig. 14.** Shear sense shown by orange half arrows. a. A $\delta$ structure on a quartz vein. Since the tail and the core seem to be continuous, for such structures, using the present mathematical model is to be avoided. Location: Bhagirathi section of Greater Himalayan Crystallines, India. Reproduced from Fig. 1.4d of Mukherjee (2013b). b. A complex structure with quartz core but showing a reliable top-to-left (up) ductile shear. The tail of biotite and quartz layer at left and right show $\delta$-structure geometry. However, a $\sigma$ structure like tail is also noted (blue full arrow). Following the present work (e.g. see Fig. 8), a slip boundary condition may be a possibility in this ductile shear zone. Reproduced from Mukherjee (2014). Length of a part of the pen visible is 3 cm. c. Top-to-left sheared garnet porphyroblast. $\delta$ type (blue full arrow) and a possible $\sigma$ type (red full arrow) at a single side of the blast. This is comparable to the slip example in Fig. 11 in this work at low shear strain. Main Central Thrust/Vaikrita Thrust in the Karcham area, basal part of the GHC, Sutlej river section, Himachal Pradesh, India. Reproduced from Fig. 1.75 of Mukherjee (2013a). Cross-polarized light. Width of image: 4 mm. d. Top-to-left sheared clast showing a $\sigma$ structure. Mylonitized gneiss from Greater Himalayan Crystallines, Bhagirathi section, India. Reproduced from Fig. 1.40 of Mukherjee (2014). Length of a part of the pen visible is 7 cm. (For interpretation of the references to colour in this figure legend, the reader is referred to the web version of this article.)
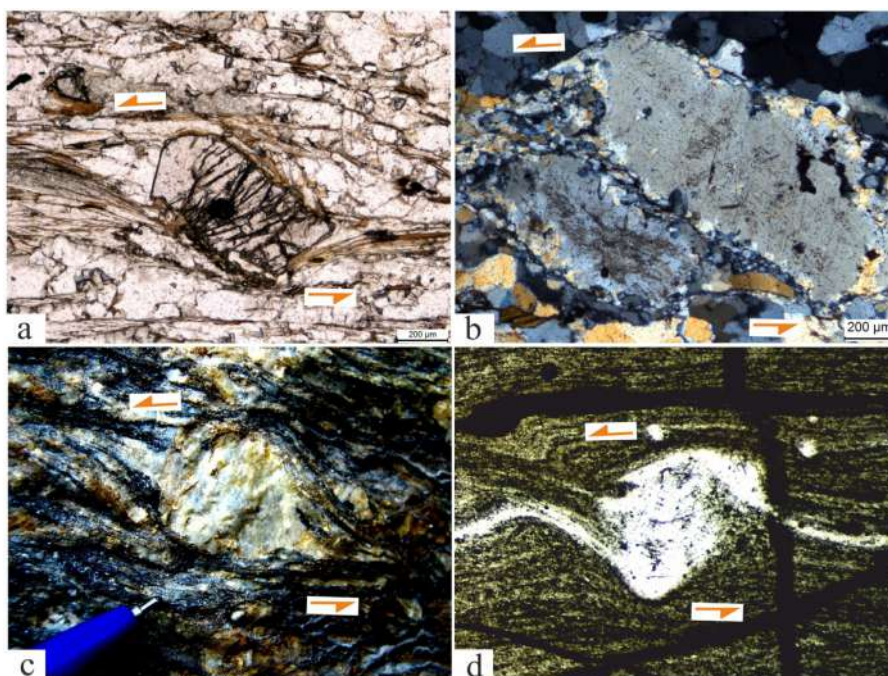


**Fig. 15.** Shear sense shown by orange half arrows. a. A top-to-left sheared and fractured garnet porphyroblast displaying a $\sigma$ geometry. A single generation of tail is noted. Photographed by Dripta Dutta. Cross-polarized light. Width of image: 0.5 mm. Location: Near Karzog (previously unpublished photomicrograph). b. Quartz grains showing top-to-left shear and $\sigma$ geometries. Recrystallized materials at the boundaries define the mantle. Photographed by Dripta Dutta. Cross-polarized light. Width of image: 0.5 mm. Location: Near Karzog (previously unpublished photomicrograph). c. Top-to-left sheared feldspar clast enveloped within sub-horizontal primary shear planes. Note the two tails are of different geometries. Greater Himalayan Crystallines, Bhagirathi section, India. Reproduced from Fig. 1.48 of Mukherjee (2014). Length of a part of the pen visible is 3.5 cm. d. A $\delta$ structure composed of olivine (reproduced from Fig. 2.42 of Mukherjee (2015)). Both the foliated matrix and the tail are folded. Photo width: 0.25 mm.
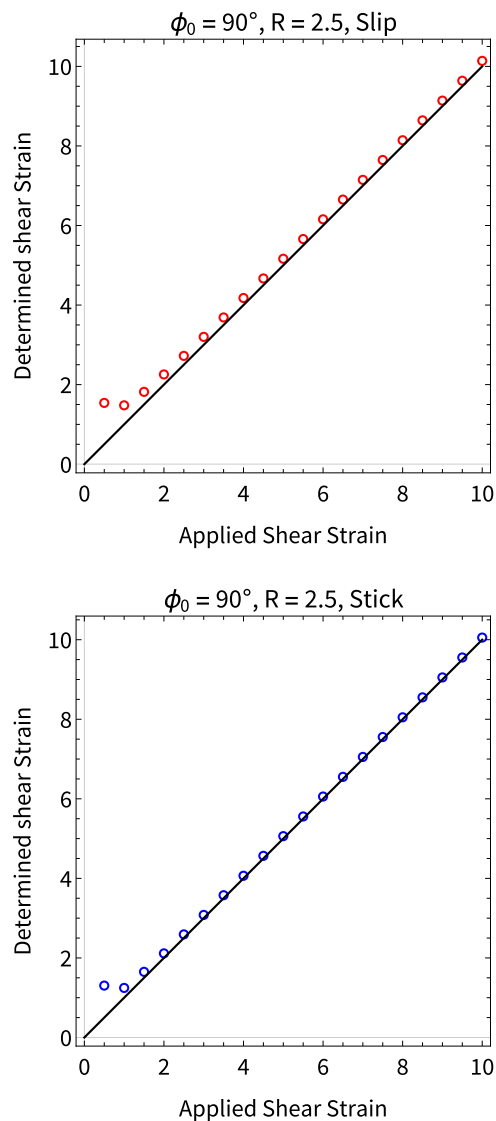
**Fig. 16.** Results of calculating shear strain from the tips of mantle wings using numerical data.

other, clearer examples to deduce the shear sense of the deformed rock. Additionally, if most objects in an outcrop demonstrate a consistent synthetic orientation with respect to the direction of shear (e.g. Pennacchioni et al. (2000)), then this is likely to support interpreting the sense of shear from this observation. Given that the slip boundary condition results in stable synthetic object orientations despite ongoing deformation (Mulchrone, 2007a) then it is likely that these objects deformed under slip conditions.

### Declaration of competing interest

The authors declare that they have no known competing financial interests or personal relationships that could have appeared to influence the work reported in this paper.

### CRediT authorship contribution statement

**Kieran F. Mulchrone:** Conceptualization, Data curation, Formal analysis, Investigation, Methodology, Software, Visualization, Writing - original draft, Writing - review & editing. **Soumyajit Mukherjee:** Conceptualization, Investigation, Writing - original draft.

### References

Bellot, J.-P., Bronner, G., Laverne, C., 2002. Transcurrent strain partitioning along a suture zone in the Maures massif (France): Result of an eastern indenter tectonics in European Variscides? In: Martínez Catalán, J.R., Hatcher, R.D., Arenas Jr., R., Díaz García, F. (Eds.), Variscan–Appalachian Dynamics: The Building of the Late Paleozoic Basement. In: Geological Society of America Special Paper, vol. 364, pp. 223–237.
Bjornerud, M., 1989. Toward a unified conceptual framework for shear sense indicators. J. Struct. Geol. 11, 1045–1049.
Bons, P.D., Barr, T.D., ten Brink, C.E., 1997. The development of d-clasts in non-linear viscous materials: A numerical approach. Tectonophysics 270, 29–41.
Bose, S., Marques, F.O., 2004. Controls on the geometry of tails around rigid circular inclusions: Insights from analogue modelling in simple shear. J. Struct. Geol. 26, 2145–2156.
Boudier, F., Al-Rajhi, A., 2014. Structural control on chromite deposits in ophiolites: The oman case. In: Rollinson, H.R., Searle, M.P., Abbasi, I.A., Al Kindi, M.H. (Eds.), Tectonic Evolution of the Oman Mountains, Vol. 392. Geological Society of London, Special Publication, pp. 263–277.
Dutta, D., Mukherjee, S., 2019. Opposite shear senses: Geneses, global occurrences, numerical simulations and a case study from the Indian western Himalaya. J. Struct. Geol. 126, 357–392.
Fossen, H., Cavalcante, G.C.G., 2017. Shear zones – A review. Earth-Sci. Rev. 171, 434–455.
Fossen, H., Tikoff, B., 1993. The deformation matrix for simultaneous simple shearing, pure shearing and volume change, and its applications to transpression-transtension tectonics. J. Struct. Geol. 15, 413–422.
Frehner, M., Exner, U., Mancktelow, N.S., Grujic, D., 2011. The not-so-simple effects of boundary conditions on models of simple shear. Geology 39, 719–722.
Ghosh, S.K., Sengupta, S., 1973. Compression and simple shear of test models with rigid and deformable inclusions. Tectonophysics 17, 133–175.
Grasemann, B., Dabrowski, M., 2015. Winged inclusions: Pinch and swell objects during high-strain simple shear. J. Struct. Geol. 70, 78–94.
Griera, A., Llorens, M.-G., Gomez-Rivas, E., Bons, P.D., Jessel, M.W., Evans, L.A., Lebensohn, R., 2013. Numerical modelling of porphyroclast and porphyroblast rotation in anisotropic rocks. Tectonophysics 587, 4–29.
Hollister, L.S., Crawford, M.L., 1986. Melt-enhanced deformation: A major tectonic process. Geology 14, 558–561.
Iacopini, D., Frassi, C., Carosi, R., Montomoli, C., 2011. Biases in three-dimensional vorticity analysis using porphyroclast system: Limits and application to natural examples. Geol. Soc. Special Publ. 360, 301–318.
Ildefonse, B., Mancktelow, N.S., 1993. Deformation around rigid particles: The influence of slip at the particle/matrix interface. Tectonophysics 22, 345–359.
Ildefonse, B., Sokoutis, D., Mancktelow, N.S., 1992. Mechanical interactions between rigid particles in a deforming ductile matrix: Analogue experiments in simple shear flow. J. Struct. Geol. 14, 1253–1266.
Ishii, K., Kanagawa, K., Shigematsu, N., 2007. High ductility of K-feldspar and development of granitic banded ultramylonite in the Ryoke metamorphic belt, SW Japan. J. Struct. Geol. 29, 1083–1098.
Jeffery, G.B., 1922. The motion of ellipsoidal particles immersed in a viscous fluid. Proc. R. Soc. A 102, 201–211.
Mandal, N., Misra, S., Samanta, S.K., 2005. Rotation behaviour of rigid inclusions in multiple association: Insights from experimental and theoretical models. J. Struct. Geol. 27, 731–743.
Mandal, N., Samanta, S.K., Bhattacharyya, G., Chakraborty, C., 2003. Deformation of ductile inclusions in a multiple inclusion system in pure shear. J. Struct. Geol. 25, 1359–1370.
Mandal, N., Samanta, S.K., Chakraborty, C., 2000. Progressive development of mantle structures around elongate porphyroclasts: Insights from numerical models. J. Struct. Geol. 22, 993–1008.
Mandal, N., Samanta, S.K., Chakraborty, C., 2001. Numerical modeling of heterogeneous flow fields around rigid objects with special reference to particle paths, strain shadows and foliation drag. Tectonophysics 330, 177–194.
Marques, F.O., Mandal, N., Taborda, R., Antunes, J.V., Bose, S., 2014. The behaviour of deformable and non-deformable inclusions in viscous flow. Earth-Sci. Rev. 134, 16–69.
Marques, F.O., Taborda, R., Antunes, J., 2005a. Influence of a low-viscosity layer between rigid inclusion and viscous matrix on inclusion rotation and matrix flow: A numerical study. Tectonophysics 407, 101–115.
Marques, F.O., Taborda, R., Bose, S., Antunes, J., 2005b. Effects of confinement on matrix flow around a rigid inclusion in viscous simple shear: Insights from analogue and numerical modelling. J. Struct. Geol. 27, 379–396.

Mukherjee, S., 2011. Mineral Fish: Their morphological classification, usefulness as shear sense indicators and genesis. Int. J. Earth Sci. 100, 1303–1314.

Mukherjee, S., 2012. Simple shear is not so simple! Kinematics and shear senses in Newtonian viscous simple shear zones. Geol. Mag. 149, 819–826.

Mukherjee, S., 2013a. Deformation Microstructures in Rocks. Springer Geochemistry/Mineralogy, Berlin, pp. 1–111.

Mukherjee, S., 2013b. Higher Himalaya in the Bhagirathi section (NW himalaya, India): Its structures, backthrusts and extrusion mechanism by both channel flow and critical taper mechanisms. Int. J. Earth Sci. 102, 1851–1870.

Mukherjee, S., 2014. Atlas of Shear Zone Structures in Meso-Scale. Springer Geology, Berlin, pp. 1–124.

Mukherjee, S., 2015. Atlas of Structural Geology. Elsevier, Amsterdam, pp. 55, 70.

Mukherjee, S., 2017. Review on symmetric structures in ductile shear zones. Int. J. Earth Sci. 106, 1453–1468.

Mukherjee, S., Mulchrone, K.F., 2012. Estimating the viscosity and Prandtl number of the Tso Morari Gneiss Dome, western Indian Himalaya. Int. J. Earth Sci. 101, 1929–1947.

Mulchrone, K.F., 2007a. An analytical solution in 2D for the motion of rigid elliptical particles with a slipping interface under a general deformation. J. Struct. Geol. 29, 950–960.

Mulchrone, K.F., 2007b. Modelling flanking structures using deformable high axial ratio ellipses: Insights into finite geometries. J. Struct. Geol. 29, 1216–1228.

Mulchrone, K.F., Mukherjee, S., 2016. Kinematics and shear heat pattern of ductile simple shear zones with 'slip boundary condition'. Int. J. Earth Sci. 105, 1015–1020.

Mulchrone, K.F., Mukherjee, S., 2019. Kinematics of ductile shear zones with deformable or mobile walls. J. Earth Syst. Sci. 128, 218.

Mulchrone, K.F., Walsh, K., 2006. The motion of a non-rigid ellipse in a general 2D deformation. J. Struct. Geol. 28, 392–407.

Odonne, F., 1994. Kinematic behaviour of an interface and competence contrast: Analogue models with different degrees of bonding between deformable inclusions and their matrix. J. Struct. Geol. 16, 997–1006.

Passchier, C.W., 1984. The generation of ductile and brittle shear bands in a low angle mylonite zone. J. Struct. Geol. 6, 273–281.

Passchier, C.W., ten Brink, C.E., Bons, P.D., Sokoutis, D., 1993. Delta-objects as a gauge for stress sensitivity of strain rate in mylonites. Earth Planet. Sci. Lett. 120, 239–245.

Passchier, C.W., Simpson, C., 1986. Porphyroclast systems as kinematic indicators. J. Struct. Geol. 8, 831–843.

Passchier, C.W., Sokoutis, D., 1993. Experimental modelling of mantled porphyroblasts. J. Struct. Geol. 7, 895–909.

Passchier, C.W., Trouw, R.A.J., 2005. Microtectonics, second ed. Springer, Berlin, p. 139.

Pennacchioni, G., Fasolob, L., Cecchi, M.M., Salasniche, L., 2000. Finite-element modelling of simple shear fow in Newtonian and non-Newtonian fuids around a circular rigid particle. J. Struct. Geol. 22, 683–692.

Ramsay, J.G., 1980. Shear zone geometry: A review. J. Struct. Geol. 2, 83–99.

Regenauer-Lieb, K., Yuen, D.A., 2003. Modeling shear zones in geological and planetary sciences: Solid- and fluid-thermal–mechanical approaches. Earth Sci. Rev. 63, 295–349.

Samanta, S.K., Mandal, N., Chakraborty, C., 2003. Flow patterns around rigid inclusions in a multiple inclusion system undergoing bulk simple shear deformation. J. Struct. Geol. 25, 209–221.

Schlichting, H., Gersten, K., 1999. Boundary Layer Theory. 8th revised enlarged edition. Springer, Berlin.

Schmid, D.W., Podladchikov, Y.Y., 2005. Mantled porphyroclast guages. J. Struct. Geol. 27, 571–585.

Schrank, C.E., Boutelier, D.A., Cruden, A.R., 2008. The analogue shear zone: From rheology to associated geometry. J. Struct. Geol. 30, 177–193.

Tikoff, B., Fossen, H., 1993. Simultaneous pure and simple shear: The unifying deformation matrix. Tectonophysics 217, 267–283.

Tikoff, B., Fossen, H., 1995. The limitations of three dimensional kinematic vorticity analysis. J. Struct. Geol. 17, 1771–1784.

Tikoff, B., Fossen, H., 1999. Three dimensional reference deformations and strain facies. J. Struct. Geol. 21, 1497–1512.

Trouw, R.A.J., Passchier, C.W., Wiersma, D.J., 2010. Atlas of Mylonites and Related Microstructures. Springer, Berlin.